

Edge Detection, Cosmic Strings and the South Pole Telescope

Andrew Stewart* and Robert Brandenberger†

Physics Department, McGill University, Montreal, QC, H3A 2T8, CANADA

(Dated: October 30, 2018)

We develop a method of constraining the cosmic string tension $G\mu$ which uses the Canny edge detection algorithm as a means of searching CMB temperature maps for the signature of the Kaiser-Stebbins effect. We test the potential of this method using high resolution, simulated CMB temperature maps. By modeling the future output from the South Pole Telescope project (including anticipated instrumental noise), we find that cosmic strings with $G\mu > 5.5 \times 10^{-8}$ could be detected.

I. INTRODUCTION

At very early times it is believed that the universe underwent a series of symmetry breaking phase transitions which led to the formation of different types of topological defects. Among them are linear topological defects known as cosmic strings (for reviews see e.g. [1, 2, 3]). After creation, the cosmic strings form a random network of infinite strings and closed string loops, the arrangement of which evolves over time through string interactions. Cosmic strings can also have self-interactions that lead to the formation of closed loops via the exchanging of endpoints, or *intercommutation* [4]. When formed, cosmic string loops break off of the longer segments and continue to oscillate, losing energy via gravitational radiation, until eventually decaying. Infinitely long strings, on the other hand, cannot decay into gravitational radiation and survive indefinitely. The string network eventually approaches a scaling regime in which the number of strings crossing a given Hubble volume is fixed and the strings contribute some fraction of the total energy in the universe. The existence of a scaling solution is supported by independent numerical simulations of the evolution of the cosmic string network [5, 6, 7, 8]. The quantity which characterizes the cosmic strings is their tension, μ , which is equivalent to the mass per unit length. This tension is directly determined by the energy scale of the symmetry breaking during which the cosmic strings were formed. It is possible that cosmic strings could have been formed at many different epochs, meaning the tension of the cosmic strings can take a wide variety of values. When discussing cosmic strings it

*stewart@physics.mcgill.ca

†rhb@physics.mcgill.ca

is more common to work with the dimensionless parameter $G\mu$, where G is Newton's constant. Until the late 1990's, cosmic strings were studied as potential seeds for structure formation [9, 10, 11]. The eventual discovery of the acoustic peaks [12, 13] in the angular power spectrum of the CMB lead to cosmic strings being ruled out as the main origin of structure in favour of the inflationary paradigm, since the angular power spectrum predicted by cosmic strings consists of only a single broad peak [14, 15, 16]. Despite this, there currently exists a renewed interest in cosmic strings fueled by the study of different cosmological models in which their formation is generically predicted (see [17, 18, 19] for just a few possibilities). It has also recently been shown that a contribution of less than 10% of the observed CMB power on large scales coming from cosmic strings is acceptable [20, 21, 22, 23, 24, 25, 26].

The current bounds on the cosmic string tension come from a variety of measurements. The gravitational waves emanating from many string loops at different times produce a stochastic background which is the focus of current interferometer and pulsar timing experiments. Pulsar timing, specifically, places a bound $G\mu < 10^{-7} - 10^{-8}$ on the cosmic string tension [27, 28]. However, we note that in order to place a bound on $G\mu$ using gravitational wave constraints one must make assumptions about the size of the loops which are formed in the string network, the probability that strings will intercommute when crossing, and even the string model under consideration. Whereas the scaling solution for the long string network is well established, the distribution of loops is uncertain by several orders of magnitude. Therefore, the strength of the bounds obtained by considering gravitational radiation from string loops can be questioned. A more robust bound on the tension comes from the angular power spectrum of the CMB (since the spectrum obtains an important contribution from the long string network). Assuming a scaling solution of the long string network with the parameters from numerical studies of cosmic string evolution, the string contribution to the angular power spectrum of the CMB was determined, and the results of these studies translate directly into a bound $G\mu < 5 \times 10^{-7}$ [20, 29].

Along with the above mentioned phenomena, there exists another observational signature unique to cosmic strings which could be directly detected, namely, linear discontinuities in the temperature of the CMB. This signature was first studied by Kaiser and Stebbins [30] and is usually referred to as the KS-effect. This effect occurs because the space-time around a straight cosmic string is flat, but with a wedge, whose vertex lies along the length of the string, removed. The angle subtended by the missing wedge, ϕ , is determined by the tension of the cosmic string as [31]

$$\phi = 8\pi G\mu. \tag{1}$$

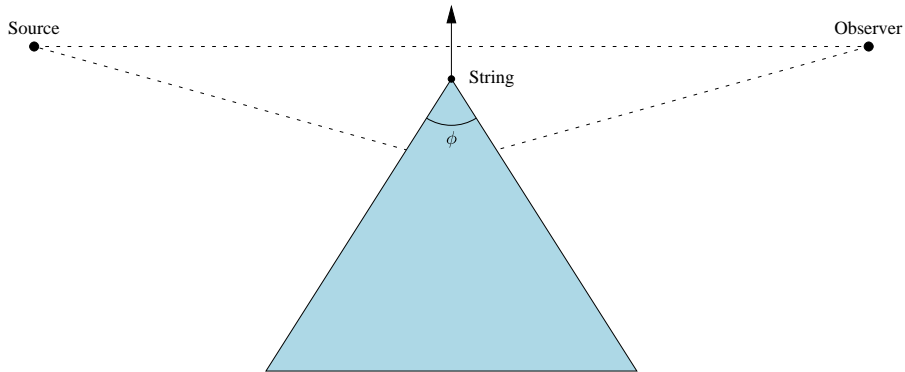


FIG. 1: The geometry of the space-time near a cosmic string. Shown here is a slice of the space-time perpendicular to the orientation of the string. The coloured area represents a missing wedge with deficit angle ϕ , while the dashed lines represent the paths of photons travelling from a source to an observer and the arrow shows the direction of motion of the string.

For an observer looking at a source while a cosmic string is moving transversely through the line of sight between the two, the photons passing from the source to the observer along one side of the string will appear to be Doppler shifted relative to those passing along the other side due to this non-trivial geometry (see Figure 1). If the source that the observer is viewing happens to be the CMB, this effect will manifest itself as discontinuities in the microwave background temperature along curves in the sky where strings are located. The magnitude of the step in temperature across a cosmic string is

$$\frac{\delta T}{T} = 8\pi G\mu\gamma_s v_s |\hat{k} \cdot (\hat{v}_s \times \hat{e}_s)|, \quad (2)$$

where v_s is the speed with which the cosmic string is moving, γ_s is the relativistic gamma factor corresponding to the speed v_s , \hat{v}_s is the direction of the string movement, \hat{e}_s is the orientation of the string and \hat{k} is the direction of observation [32]. For cosmic strings formed in a phase transition in the early universe, the “missing wedge” produced by a string has, at time t , a finite depth given by the Hubble radius $H^{-1}(t)$ at that time [33]. Some work has already been dedicated to searching for the KS-effect in current CMB data [34, 35], but a cosmic string signal was not found, leading to a constraint on the tension $G\mu \lesssim 4 \times 10^{-6}$.

In this work we implement a method of detecting the temperature discontinuities in the CMB produced by cosmic strings via the KS-effect using an edge detection algorithm commonly employed in image analysis, the Canny algorithm [36]. The motivation behind this choice is clear since the cosmic strings literally appear as edges in the CMB temperature. Depending on the sensitivity

of the edge detection algorithm to the temperature edges, a bound on the cosmic string tension could then be imposed. This work is a continuation of a previous study [37] which indicated that an edge detection method may lead to a significant improvement in the sensitivity to the presence of cosmic strings compared to previous direct searches for strings in the CMB. In this paper we improve the method proposed in [37] and we investigate its application to surveys with a different set of specifications than those examined in that initial work.

We are interested in the cosmic strings in the network that survive until later times. The times relevant to the production of an edge signature in the CMB are the time of last scattering until the present day. Based on the evolution of the network, cosmic strings are more numerous around the time of last scattering than later times. On today's sky, those strings correspond to an angular scale of approximately 1° . Therefore, an observation of the CMB with an angular resolution significantly less than 1° is necessary in order to be able to detect the edges related to these strings. With this in mind, we also focus on the application of the edge detection method to high resolution surveys of the CMB, particularly the future data from the South Pole Telescope.

The South Pole Telescope (SPT) [38] is a 10m diameter telescope being deployed at the South Pole research station. The telescope is designed to perform large area, high resolution surveys of the CMB to map the anisotropies. The SPT is designed to provide $1'$ resolution in the maps of the CMB, making it ideal to search for the KS-effect. Based on previous results [37], we believe that with such high resolution data our method could provide bounds on the cosmic string tension competitive with those of pulsar timing.

The remainder of this paper is arranged as follows: In section II, we discuss the CMB maps used in our analysis with a focus on the anisotropies coming from Gaussian fluctuations and cosmic strings. In Section III, we outline the edge detection algorithm we are using, highlighting the details of our particular implementation. In Section IV, we discuss how we quantify the edge maps output by the edge detection algorithm and we explain the statistical analysis used to determine if a significant difference has been detected. In Section V, we present the results of running the edge detection algorithm on CMB maps and the possible constraints on the cosmic string tension that could be applied. We finish in Section VI with a discussion of our results.

II. MAP MAKING

For this initial investigation of edge detection as a method for constraining or even detecting cosmic strings, we generate CMB temperature anisotropy maps by means of numerical simulations

and use these as the input for the edge detection algorithm. The simulated maps are constructed through the superposition of different temperature anisotropy components based on the type of effects being reproduced. We are interested in the simulation of small angular scale patches of the microwave sky, so we employ the flat-sky approximation [39]. In this approximation, the geometry of a small patch on the sky can be considered to be essentially flat. Thus, each map component, as well as the final map itself, is a two dimensional square image characterized by an angular size and an angular resolution. Specifically, we work with a square grid that has a size corresponding to the angular size being simulated, and a pixel size corresponding to the angular resolution being simulated. The pixels in the grid are indexed by two dimensional Cartesian coordinates (x, y) and we take the upper left corner of the grid to be the origin.

The common component in every simulated CMB map is a set of temperature anisotropies produced by Gaussian inflationary fluctuations. We simulate these Gaussian fluctuations such that they account for all of the observed power in the CMB. Thus, in the absence of any other sources the final simulated map is simply equivalent to the Gaussian component and is consistent with observations. That is, we define

$$T(x, y) \equiv T_G(x, y), \quad (3)$$

where $T(x, y)$ represents the the final temperature anisotropy map and $T_G(x, y)$ represents the Gaussian component.

To make a CMB map including the effects of cosmic strings, we simulate a separate component of string induced temperature fluctuations produced via the KS-effect. In linear perturbation theory, if there are two sources of fluctuations, the resulting temperature anisotropies are given by a linear superposition of the individual sources. Therefore, the total temperature map is obtained by simply summing the contributions from Gaussian noise and from cosmic strings. Note, however, that the power of the Gaussian component must be adjusted in order to obtain the total observed power of CMB fluctuations. That is, if $T_G(x, y)$ is the WMAP-normalized Gaussian signal, then, in a map including cosmic strings, it needs to be reduced by a scaling factor α , the value of which is determined by the tension of the cosmic strings being simulated. Denoting the string component by $T_S(x, y)$, the total temperature map is

$$T(x, y) \equiv \alpha T_G(x, y) + T_S(x, y). \quad (4)$$

In this way the strings can contribute a fraction of the total power, while the final map is still in agreement with current measurements of the angular power spectrum of CMB anisotropies.

Let us comment in more detail on the nature of this scaling. We demand that the angular power of the final combined temperature map match the observed angular power for multipole values up to the first acoustic peak, i.e. $l \lesssim 220$. We choose this multipole range because it is tightly constrained by current observations [40]. However, as mentioned above, the Gaussian component alone accounts for all of the observed angular power in the CMB. Thus, this demand is equivalent to requiring that the angular power of the combined map match that of a pure Gaussian component. Working in the flat-sky approximation allows us to replace the usual spherical harmonic analysis of the CMB fluctuations by a Fourier analysis [39]. We can then express our condition as

$$\langle |T_G(k < k_p)|^2 \rangle = \alpha^2 \langle |T_G(k < k_p)|^2 \rangle + \langle |T_S(k < k_p)|^2 \rangle, \quad (5)$$

where k_p is the wavenumber corresponding to the first acoustic peak of the angular power spectrum of the CMB, $\langle |T_S(k < k_p)|^2 \rangle$ is the average of the Fourier temperature anisotropy values from the string component for wavenumbers less than k_p and $\langle |T_G(k < k_p)|^2 \rangle$ is the equivalent object for the Gaussian component. From Equation (2) one can see that the average of the temperature anisotropy values in the string component should go as the cosmic string tension squared. Therefore, if we define a reference cosmic string tension, $G\mu_0$, we have

$$\langle |T_S(k < k_p)|^2 \rangle = \langle |T_S(k < k_p)|^2 \rangle_0 \left(\frac{G\mu}{G\mu_0} \right)^2, \quad (6)$$

where $\langle |T_S(k < k_p)|^2 \rangle_0$ is the average for a string component corresponding to the reference tension and $G\mu$ is the cosmic string tension corresponding to the string component on the left-hand side of the equation. Substituting this into (5) we can solve for the final form of the scaling factor:

$$\alpha^2 = 1 - \frac{\langle |T_S(k < k_p)|^2 \rangle_0}{\langle |T_G(k < k_p)|^2 \rangle} \left(\frac{G\mu}{G\mu_0} \right)^2. \quad (7)$$

The benefit of having α in this form is we need only calculate the ratio of averages once using the reference tension. After this we can calculate the value of the scaling factor with only the cosmic string tension used in the given simulation, $G\mu$. As mentioned in the Introduction, studies of combining string anisotropies and Gaussian anisotropies [21, 22] have concluded that, on the basis of the angular power spectrum of CMB anisotropies, a cosmic string contribution of less than 10% of the observed CMB power on large scales cannot be ruled out in general. However, in calculating the angular power spectrum, coherent features in position space such as the line discontinuities induced by the Kaiser-Stebbins effect are washed out. Thus, we expect that better limits on the string tension can be established by making use of edge detection algorithms working in position space.

A third component which we must include in the final map is a simulation of instrumental noise. For simplicity, we simulate an instrumental noise component that is simply white noise with some given maximum amplitude in the temperature difference $\delta T_{N,max}$. If an instrumental noise component is included we do not need to perform any additional scaling of the initial Gaussian component of the map since the instrumental noise does not modify the actual sky map. Thus, the instrumental noise component is simply summed directly to the other components. Denoting the noise component by $T_N(x, y)$, we have

$$T(x, y) \equiv T_G(x, y) + T_N(x, y) \quad (8)$$

for a simulation without cosmic strings, or

$$T(x, y) \equiv \alpha T_G(x, y) + T_S(x, y) + T_N(x, y) \quad (9)$$

for a simulation including cosmic strings.

The dominant portion of the final simulated map is the Gaussian temperature fluctuations. As such, these Gaussian fluctuations represent the most significant “noise” when trying to directly detect the effect of cosmic strings with the edge detection algorithm. The significance of the instrumental noise component in the final map is determined by the maximum amplitude of the noise, which should in general be small compared to the amplitude of the Gaussian fluctuations. The size of the temperature anisotropies in the string component depends directly on the tension of the cosmic strings which are being simulated, as described by Equation (2). For interesting values of the string tension, the amplitude of the string-induced anisotropies will lie from a factor of a few up to orders of magnitude below the amplitude of the Gaussian temperature anisotropies, thus presenting the difficulty in directly detecting them. Examples of each of the three map components are shown in Figure 2. Before moving on to discuss the edge detection algorithm itself, we first review our methods for generating the Gaussian and string components.

A. The Gaussian Component

As touched on above, the spherical harmonic expansion of the CMB temperature anisotropies can be replaced by a Fourier expansion when using the flat-sky approximation [39]. Therefore, when generating the component of Gaussian fluctuations, we choose to work on a grid in Fourier space where each pixel in the grid is indexed by the coordinates (k_x, k_y) , which are the components of the wavevector pointing to that pixel. The size and resolution of the grid still correspond to the

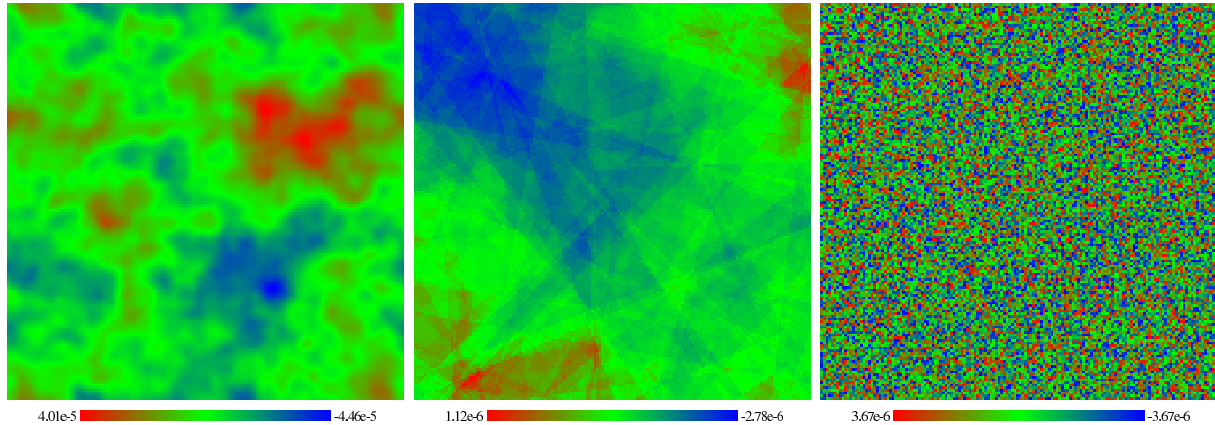


FIG. 2: Components of a simulated temperature anisotropy map. On the left is a component of Gaussian temperature fluctuations, in the middle is a component of cosmic string induced temperature fluctuations and on the right is a component of instrumental noise. In all three components, the angular size of the simulated region is $2.5^\circ \times 2.5^\circ$ and the angular resolution is $1'$ per pixel (22,500 pixels). In the string component the tension of the cosmic strings was taken to be $G\mu = 6 \times 10^{-8}$ and the number of strings per Hubble volume in the scaling solution was taken to be $M = 10$. The colour of a pixel represents the value of the temperature anisotropy at that pixel, as described by the scale below each image.

two angular scales in the simulation. The advantage of being able to use a Fourier analysis is that it greatly simplifies the calculations, and the value of the temperature anisotropy at a particular pixel on the the grid is then given by the relation

$$\frac{\delta T_G}{T}(k_x, k_y) = g(k_x, k_y) a(k_x, k_y), \quad (10)$$

where $g(k_x, k_y)$ is a random number taken from a normal probability distribution with mean zero and variance one [41]. The quantity $a(k_x, k_y)$ is the Fourier space equivalent of a_{lm} in the usual spherical harmonic expansion and is related to the angular power spectrum of the temperature anisotropies in the same way,

$$\langle |a(k_x, k_y)|^2 \rangle = C_l. \quad (11)$$

In the flat-sky approximation the multipole moment is related to pixel position in the grid by

$$l = \frac{2\pi}{\theta} \sqrt{k_x^2 + k_y^2}, \quad (12)$$

where θ is the angular size of the survey area [41].

We compute the Fourier temperature fluctuations pixel by pixel using the above equations. It is clear from Equation (12) that, in general, the largest multipole moment required for a simulation

increases as the resolution increases. Since we are interested in simulating high resolution CMB maps, we generate the COBE normalized angular power spectrum of the CMB to very large multipole moments using the CAMB software with input cosmological parameters determined by surveys at lower angular resolution. To be precise, we choose our input parameters to be those derived using the CMBall data set, which combines the results from multiple surveys [42]. Depending on the pixel position, the value of l as calculated by Equation (12) can take non-integer values, whereas the angular power spectrum is computed for only integer values. In these cases, we simply approximate the value of the angular power spectrum at any given l using a linear interpolation. Once we have computed the value of each pixel in the grid, we take the inverse Fourier transform of the array using a fast Fourier transform (FFT) algorithm, which produces a temperature anisotropy map in position space.

By choosing the origin of the grid to be at the top left corner in the maps, we have introduced a preferred direction into the simulation of the Gaussian fluctuations. To compensate for this asymmetry, we construct the final Gaussian component, $T_G(x, y)$, by superimposing four separate sub-components, which we label as $T_1...T_4$, each computed separately using the method described above. When combining these sub-components, we reflect each along one of the four axes on the grid eliminating any irregularity in the final map. Therefore, the Gaussian component is defined as

$$T_G(x, y) \equiv \frac{1}{2} [T_1(x, y) + T_2(x_{max} - x, y) + T_3(x, y_{max} - y) + T_4(x_{max} - x, y_{max} - y)], \quad (13)$$

where x_{max} and y_{max} are the maximal x and y values based on the simulation parameters. The factor of $1/2$ in front of the sum is required to maintain the original standard deviation.

B. The String Component

Since the focus of this work is on testing the edge detection method, not the details of the cosmic string network evolution, we utilize a toy model of the network for simplicity. We then examine the resulting temperature anisotropies caused by the strings which photons encounter between the time of last scattering and the present day. We choose to use the toy model originally presented by Perivolaropoulos in [43].

In this model, we first separate the period between the present time, t_0 , and the time of last scattering, t_{ls} , into N Hubble time steps such that $t_{i+1} = 2t_i$. For a redshift of last scattering

$z_{ls} = 1000$ we then have [32]

$$N = \log_2 \left(\frac{t_0}{t_{ls}} \right) \simeq 15. \quad (14)$$

For large redshifts and assuming $\Omega_0 = 1$, the angular size of the Hubble volume at a given Hubble time is approximated by $\theta_{H_i} \sim z_i^{-1/2} \sim t_i^{1/3}$. Therefore, we have $\theta_{H_{ls}} \simeq z_{ls}^{-1/2} \simeq 1.8^\circ$ for the Hubble volume corresponding to the time of last scattering and $\theta_{H_{i+1}} \simeq 2^{1/3} \theta_{H_i}$ for all subsequent Hubble time steps [32]. At each Hubble time, a network of long straight strings with a length equal to two times the size of the Hubble volume at that time, each with random position, orientation and velocity, is laid down. The network of strings produced at each Hubble time is assumed to be uncorrelated with that of the previous Hubble time. This is justified since cosmic strings move with relativistic speeds, meaning that between Hubble times there will be multiple string interactions, causing the network to enter into a completely different configuration.

For a specific Hubble time step t_i we start with an extended region that has a total angular size equivalent to the angular size of the string component being simulated plus two times the angular size of the Hubble volume at that particular Hubble time. The number of strings n_i that should exist in that particular region is then given by the scaling solution

$$n_i = M \frac{(\theta + 2\theta_{H_i})^2}{\theta_{H_i}^2}, \quad (15)$$

where M is the number of cosmic strings crossing each Hubble volume and θ is the angular size of the string component being simulated [32]. As usual, we work on a square grid, this time placed over the entire extended region, with pixel size still given by the angular resolution being considered. Pixels within the entire extended area are then chosen at random to be the midpoints of strings, with a probability such that the average number of strings in a single Hubble volume is in agreement with the number M of the scaling solution. If a pixel is chosen to be a midpoint, we choose a random orientation about that pixel and we place a straight string of length $2\theta_{H_i}$. We then simulate the temperature fluctuation produced by that string by adding a temperature anisotropy

$$\frac{\delta T_S}{T} = 4\pi G\mu\gamma_s v_s r \quad (16)$$

to a rectangular region on one side of the string, and subtracting the same amount from a rectangular region on the other side. This temperature anisotropy corresponds to the KS-effect as given by Equation (2), where $r = |\hat{k} \cdot (\hat{v}_s \times \hat{e}_s)|$ takes into account the projection effects. The direction of observation \hat{k} is approximately constant over the entire field of view while the quantity $\hat{v}_s \times \hat{e}_s$ is a

random unit vector since both the string orientation and velocity are random. Thus, the value of r is uniformly distributed over the interval $[0,1]$ [32]. In Equation (16), we take the RMS speed of the strings to be $v_s = 0.15$ [32], so the amplitude of the fluctuation is determined entirely by the string's tension and its orientation. Each rectangular region affected by the temperature fluctuation has a length $2\theta_{H_i}$ along the direction of the string and extends a distance θ_{H_i} in the direction perpendicular to the string [33]. Thus, each cosmic string gives rise to five separate temperature discontinuities: one at its position, two parallel to it at a distance θ_{H_i} and two perpendicular to the string at the endpoints. After placing all of the cosmic strings and calculating the temperature fluctuation for each, we have finished simulating the cosmic string network for the given time step.

Since we began with a region which is larger than the string component we wanted to simulate in the first place, we must crop the larger area to the correct size. We choose to discard pixels equally from all four sides of the extended area, so that we retain only those from the central region of the larger area. By identifying the correctly sized simulated area with the centre of the extended area, one can see that what we essentially did when first defining the extended region was to enlarge the actual simulation area by a Hubble volume in each direction. The reason that we expand our simulated area in this way is because any string whose midpoint is within a distance θ_{H_i} of the actual area we want to simulate could enter into it. Thus, we must also account for these strings which lie around the edges of the area of interest, not only those centred within it.

The final string-induced anisotropy map is given by the superposition of the effects of all of the strings in all of the Hubble volumes. Therefore, to produce the final cosmic string component $T_S(x, y)$, we simply sum together all fifteen sub-components pixel by pixel. This superposition approximates the contribution from the entire, more complex cosmic string network.

In the model described above, we have fixed values for the the speed of the strings, the length of the strings and the depth of the rectangular temperature fluctuation region around the string. These values were obtained from particular numerical simulations [32], however, these parameters can vary significantly for different models of the string network (see [1] for a review) and should not be considered as established. We also note that in this toy model cosmic string loops and their subsequent effects are not included. Cosmic string loops will also produce CMB anisotropies. However, based on the current knowledge of the distribution of scaling strings, the string loop contribution to the CMB is believed to be sub-dominant. This justified us neglecting these effects.

III. THE CANNY EDGE DETECTION ALGORITHM

When looking for edges in an image we are looking for curves across which there is a strong intensity contrast. The strength of an edge can then be quantified by the magnitude of the contrast from one side of the edge to the other, or equivalently, the magnitude of the gradient across the edge. For CMB temperature anisotropy maps, the intensity that we are dealing with is simply the amplitude of the fluctuations. Thus, we define the edges in the CMB maps as lines across which the temperature difference is large. To search for these edges we employ the Canny edge detection algorithm [36], which is one of the most commonly used edge detection methods in image analysis. Figure 3 shows an example of a final map of edges generated by the Canny algorithm along with an intermediate map produced during the edge detection process. To clearly illustrate the result of each stage of the edge detection, we present maps corresponding to the same cosmic string component shown in Figure 2 with no other components added to it, however, this does not represent a legitimate final simulated CMB map. In the following sections we review the steps involved in applying the Canny algorithm to CMB maps and how these images are generated.

A. Non-maximum Suppression

Since we are interested in temperature gradients, the first step of the Canny edge detection algorithm is to simply compute the gradient of the temperature anisotropy map and use it to determine which pixels could be part of an edge. We first construct two square filters $F_x(x, y)$ and $F_y(x, y)$, which are first-order derivatives of a two dimensional Gaussian function along each of the two map coordinates (x, y) . We then apply each of these filters to the temperature map separately by convolving the two using a FFT. This produces two new maps $G_x(x, y)$ and $G_y(x, y)$, which are the components of the gradient magnitude along the x -direction and y -direction. With these components we can then construct another new map

$$G(x, y) = \sqrt{G_x^2(x, y) + G_y^2(x, y)}, \quad (17)$$

which is the map of the gradient magnitude, or edge strength, corresponding to the original temperature anisotropy map. We can also construct a second map

$$\theta_G(x, y) = \arctan\left(\frac{G_y(x, y)}{G_x(x, y)}\right), \quad (18)$$

which is the map of the gradient angle, or gradient direction. In the above equation the sign of both components is taken into account so that the angle is placed in the correct quadrant. Therefore,

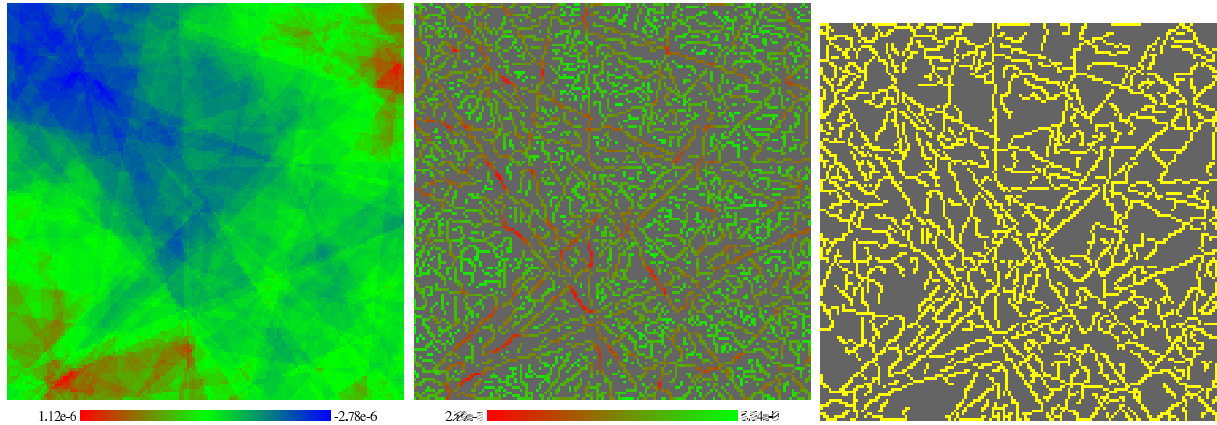


FIG. 3: Maps produced by the Canny edge detection algorithm. On the left is a temperature anisotropy map that consists of cosmic string induced fluctuations only. The colour of a pixel represents the magnitude of the temperature anisotropy as described by the scale below the image. In the middle is an example of a map of local maxima generated after non-maximum suppression. The size of the gradient filters used was 5×5 pixels. The colour of a pixel represents the magnitude of the gradient at that pixel, as described by the scale below the image. On the right is an example of a final map of edges generated after thresholding with hysteresis. The values of the thresholds used were $t_u = 0.25$, $t_l = 0.10$ and $t_c = 3.5$. The value of G_m was calculated using a cosmic string tension of $G\mu < 6 \times 10^{-8}$. The yellow pixels represent pixels which were determined to be on an edge. Together, these pixels show the the position, length and shape of the edges occurring in the original temperature anisotropy map. In last two maps, the grey pixels represent pixels which were discarded from the image.

the arctangent has a range of $(-180^\circ, 180^\circ]$. However, at each pixel on a square grid there are only eight distinguished directions which form four axes. In order to relate the gradient direction as calculated by Equation (18) to one that we can trace on the grid, we approximate the value of $\theta_G(x, y)$ at each pixel to lie along one of the eight grid directions. We do this by simply replacing the value of $\theta_G(x, y)$ with the angle corresponding to the closest grid direction. For example, if the gradient direction takes any of the values $-22.5^\circ \leq \theta_G(x, y) < 22.5^\circ$ it would be replaced by $\theta_G(x, y) = 0^\circ$.

In the Canny algorithm, part of the definition of a pixel that is considered to be on an edge is that it must be a local maximum in the gradient magnitude. By local maximum we mean that the gradient magnitude at a given pixel is larger than that of both pixels which neighbour it along the axis defined by the gradient direction at that same pixel. Using the gradient magnitude and direction maps, it is straightforward to check the local maximum condition pixel by pixel and determine which could be a part of an edge and which could not be part of an edge. Since we are

only interested in constructing a final map of edges, if a pixel does not satisfy the local maximum condition we immediately discard that pixel. Therefore, this process is referred to as *non-maximum suppression*.

Figure 3 shows a gradient magnitude map after non-maximum suppression has been performed. Many of the original pixels have been discarded, as expected, and we are left with a rough map of edges. Although curves corresponding to certain edges in the original temperature anisotropy component can be seen, there are many other pixels marked as local maxima corresponding to extremely weak edges, making the signal from stronger edges difficult to detect.

B. Thresholding with Hysteresis

When performing non-maximum suppression we only compared a single pixel with two of its neighbours to determine if it could be part of an edge. Pixels with a small gradient magnitude may have still been marked as a local maxima if the gradient magnitudes of their neighbours were also small. As mentioned above, Figure 3 shows that this is indeed the case. The magnitude at such pixels can in fact be so small that we do not want to consider them as edge pixels, since they can dilute the more significant signal coming from stronger edges. In addition, we want to detect edges which appear due to cosmic strings via the KS-effect. Therefore, we expect the gradient direction to be consistent across the length of the string induced edge. This directionality needs to be taken into account to determine which local maxima pixels belong to the same string edge. Taking these two points into consideration, we must further expand our definition of exactly what constitutes an edge pixel.

The Canny algorithm outlines a process of applying multiple thresholds to define the edges in an image, known as *thresholding with hysteresis*. First, we choose an upper gradient threshold, $t_u < 1$, such that we can then define a pixel which is definitely part of an edge, which we name a *true-edge pixel*, as one which is not only a local maximum but also satisfies

$$G(x, y) \geq t_u G_m. \quad (19)$$

Here G_m is the mean maximum gradient magnitude computed from simulated temperature maps which contain only strings. The value of G_m depends on the parameters of the simulation being performed, most notably the string tension, and must be computed separately for each parameter set using a selected number of simulated string maps. One can think of G_m as representing the strongest possible edge that could be formed by cosmic strings alone. Therefore, with this threshold,

we are simply stating that if the gradient magnitude at a given pixel is some chosen fraction of the maximum possible, then it must be a true-edge pixel.

It is not sufficient, however, to define the edges using only one threshold because the gradient magnitude can fluctuate at each pixel along the length of an edge. This variation can be caused by both instrumental noise and the random nature of the Gaussian anisotropies. If we applied only an upper threshold, we would reject the pixels at which the gradient magnitude fluctuates below that threshold, but should in fact still be considered as a part of a given edge. This would lead to edges being cut into smaller segments, making them look like dashed lines, rather than continuous curves on the map. To avoid this, we also choose a lower gradient threshold, $t_l < t_u$, and define a pixel which is possibly part of an edge, which we name a *semi-edge pixel*, as a local maximum pixel satisfying

$$t_l G_m \leq G(x, y) < t_u G_m. \quad (20)$$

If a local maximum pixel still falls below the lower threshold then it is immediately rejected. The latter case is the requirement that an edge pixel have some minimum strength, and cures the problem of a local maxima with extremely small gradient magnitudes being included in the final edge map.

Since we are interested in edges appearing due of the presence of cosmic strings, we also apply a ‘‘cutoff’’ threshold such that we reject all pixels for which

$$G(x, y) > t_c G_m, \quad (21)$$

where $t_c \geq 1$. We apply this third threshold because the Gaussian temperature fluctuations in the CMB map dominate those coming from the cosmic strings. As such, they lead to edges with much stronger gradient magnitudes, that is, greater than G_m . If we only applied the upper bound t_u , these edges would overwhelm the edge detection algorithm, washing out the cosmic string signal. By setting a cutoff threshold, we can discard the pixels with a gradient magnitude which we consider to be too strong to have been caused by cosmic strings, and keep only those representing the cosmic string signature. We choose $t_c \geq 1$ because we also consider the slight enhancement of weak edges corresponding to Gaussian fluctuations, as a result of the underlying cosmic string edges, to be part of the cosmic string signal.

After applying the thresholds as described above, we then further assert that any semi-edge pixel which is in contact with a true-edge pixel and has the appropriate gradient directionality is also a true-edge pixel sharing the same edge. By in contact, we mean that it is a semi-edge

pixel which is one of the six neighbouring pixels of the true-edge pixel which does not lie along the gradient direction calculated at the position of the true-edge pixel. This definition stems from the fact that the two directions perpendicular to the gradient axis represent the edge axis, while the remaining four directions represent the two axes which are next to parallel to the edge axis. Essentially, we are stating that in order to be considered part of the same edge the semi-edge pixel must lie along (or almost along) the edge axis and it would be inconsistent for a pixel sharing the same edge to lie along the gradient direction. By appropriate gradient directionality, we mean that the semi-edge pixel also has a gradient direction which is parallel or next to parallel to the gradient direction calculated at the position of the true-edge pixel. The comparison of the gradient directions represents our demand that the temperature gradient be consistent along an entire edge.

We scan the remaining pixels in the map to check which semi-edge pixels satisfy the above conditions. The ones which do are immediately changed to true-edge pixels. This allows us to fill the gaps which occur between true-edge pixels due to both types of noise, and avoid the incorrect breaking up of edges. Once a semi-edge pixel has been changed to a true-edge pixel it may then have another semi-edge pixel neighbouring it which needs to be changed, and so on. The scanning technique takes this into account and any connected series of semi-edge pixels will all be correctly changed to true-edge pixels ensuring that the entire edge is correctly identified. After scanning the map we consider all of the edges in the map to have been traced. At this point, if a pixel is still marked as a semi-edge pixel, we assume that it is not in contact with a true-edge pixel in any way, and it is rejected. The edge detection process is then finished, and the end result is the final map of true-edge pixels corresponding to the original temperature anisotropy map.

Figure 3 shows a final edge map after thresholding with hysteresis has been performed. Many of the pixels appearing in the map of local maxima have now been rejected, especially those with very small gradient magnitudes, and the stronger edges are now much better defined. This is a direct result of applying the thresholds and directionality conditions. Comparing the original temperature anisotropy map to the final edge map, it is clear that not only is the Canny algorithm good at locating the edges which are clearly visible, but that it is also sensitive to the faint edges which are not easily detectable by eye.

IV. EDGE LENGTH COUNTING AND STATISTICAL ANALYSIS

To facilitate a comparison with edge maps generated from different input temperature anisotropy maps, we need a way to quantify each individual edge map. Since we are considering cosmic strings

as a source of edges in CMB temperature anisotropy maps, one might intuitively expect that in the presence of strings one would observe a larger number of edges of all lengths, or at least a larger number in some finite range of lengths. With this in mind, we employ a simple method of quantifying the edge maps, which is to record the length of each edge appearing in the edge map.

We define a single edge as a chain of true-edge pixels where each subsequent pixel is in contact with the previous pixel and has a similar gradient direction (both in the same sense as described in the previous section). When scanning the final edge map, we count the number of pixels appearing in each separate edge. These values are exactly the lengths of the edge in units of pixels. With this data we can then construct a histogram of the total number of edges of each possible length, which corresponds to the original temperature anisotropy map. We do not consider a single pixel to represent an edge, therefore, the minimum edge length that we include in our histograms is two pixels long. If there are any single pixels marked as edges then we simply ignore them.

After generating histograms for different input maps, we need to develop a way to compare them and look for differences. Specifically, we are looking for a change in the distribution of the total number of edges between an edge map corresponding to a simulation without cosmic strings and an edge map corresponding to a simulation with cosmic strings. However, both the Gaussian and string components in the simulated CMB temperature anisotropy maps are generated using random processes. If we were to compare two histograms generated from only one simulated temperature anisotropy map each, we would not be able to draw a very meaningful conclusion. Therefore, to make our comparison more robust, we simulate many temperature anisotropy maps with the same input parameters and perform the edge detection and length counting on each one separately. This provides a set of histograms from which we can then compute the mean number of edges of each length occurring over all the runs. We also compute the standard deviation from each mean value. In the end this provides us with a new *averaged histogram* of edge lengths that has statistical error bars. Comparing two of these averaged histograms then allows us to assign a statistical significance to the difference in the distributions. From this point on, whenever we mention a histogram we mean an averaged histogram computed using many simulations.

When comparing two histograms, we compare the mean value for each specific length separately, rather than perform a single general test based on the overall shapes of the distributions. We prefer to treat each bin separately because each has a separate standard deviation associated with it. Furthermore, we assume that the underlying values used to compute each mean are normally distributed. That way we can use Student's t-statistic to determine the significance of the difference at each length.

For two samples of equal size n , Student's t-statistic is defined as

$$t = (\bar{N}_1 - \bar{N}_2) \sqrt{\frac{n}{(\sigma_1)^2 + (\sigma_2)^2}}, \quad (22)$$

where \bar{N}_1 and σ_1 are the mean and sample standard deviation of the first sample and \bar{N}_2 and σ_2 are the mean and sample standard deviation of the second sample. Given two histograms, we compute t for each length occurring in the two histograms for which $\bar{N}_i \geq 3\sigma_i$, where $i = 1, 2$. This constraint on the lengths we consider stems from our assumption that the underlying distribution of each mean value is normal. Since it would be inconsistent to consider negative values for the total number of strings at any given length, we choose only lengths for which the total number of strings is positive definite at the 3σ level. The p-value corresponding to each t is then computed from a t-distribution with $2n - 2$ degrees of freedom.

We then combine the probabilities calculated for each length, denoted by p_L , into a single statistic which characterizes the difference between the two histograms. Using Fisher's combined probability test, we can define the new statistic χ^2 as

$$\chi^2 = -2 \sum_{L=2}^{L_m} \ln(p_L), \quad (23)$$

where L_m is the maximum length at which a p-value was computed. The final p-value corresponding to the statistic χ^2 is then determined from a chi-square distribution with $2L_m - 2$ degrees of freedom.

The final step is to compare this single p-value to a significance level ϵ to conclude whether or not the difference in the two histograms is significant. We choose to work with the customary significance level $\epsilon = 0.0027$ corresponding to 3σ of a normal distribution. If our p-value is less than ϵ we state that the difference in the two edge maps is statistically significant.

V. RESULTS

We present the results of running the Canny edge detection algorithm on simulated CMB anisotropy maps in two parts. First, we report the results for simulations which are designed to mimic the expected output from the SPT. Using these results, we determine what kind of bound on the cosmic string tension one could hope to achieve using the edge detection method on data from that survey. Second, we present the results for simulations corresponding to a hypothetical survey that has different specifications than those of the SPT. We use these results to investigate how the potential constraint on the tension changes with respect to the design of the survey.

The SPT is capable of producing a 4,000 square degree survey of the anisotropies in the CMB [38]. To replicate the same amount of sky coverage, we simulate 40 separate $10^\circ \times 10^\circ$ maps,

where the angular resolution of each of these maps is $1'$ per pixel, again matching that specified for the SPT. To test the edge detection method, we simulate two separate sets of 40 maps, the first set including the effect of cosmic strings, and the second set excluding the effect of cosmic strings. Each set of maps gives rise to a histogram of edge lengths via the edge detection and edge length counting algorithms. We then compare these two histograms using the statistical analysis described in Section IV to determine if the difference in the distributions is significant. We repeat this process for many different values of the cosmic string tension, until we can no longer identify a statistically significant difference in the two histograms. Figure 4 shows a side by side comparison of a simulated CMB map without a cosmic string component and a simulated CMB map which does include a cosmic string component. The effect of the cosmic strings in the final temperature anisotropy map is not apparent and any difference in the typical structure between the two maps is unnoticeable by eye. Figure 5, on the other hand, shows a histogram corresponding to a set of maps without a cosmic string component and a histogram corresponding to a set of maps with a cosmic string component. The two histograms show that the edge detection method is in fact able to detect a difference which is not evident by eye, with maps including strings having slightly higher mean values for certain lengths. Although the difference in histograms may not seem large, this particular example would generate a significant result.

Although the angular size and resolution of the simulation are determined by the specifications of the survey in question, the values of the other free parameters in each step of process must also be fixed. We take the number of cosmic strings per Hubble volume in all of the string component simulations to be $M = 10$ [32], regardless of the cosmic string tension. In every run of the edge detection algorithm, we choose the gradient filter length to be 5 pixels, the value of the upper threshold to be $t_u = 0.25$ and the value of the lower threshold to be $t_l = 0.10$. These values for the thresholds may appear small, but as one can see from the scale in Figure 3, the gradient magnitude in the string component can take a large range of values. Therefore, G_m can be quite a bit larger than the average gradient magnitude on a string induced edge, so we must choose low values for the thresholds in order to not throw away the entire string signal. We have not mentioned the value of the scaling factor in the map addition, α , nor the value of the cutoff threshold, t_c . The reason is, we do not fix the value of these two parameters for all of the runs. In the case of the scaling factor, its value must change for each given cosmic string tension, as described by Equation (7). The value of the cutoff threshold, on the other hand, is chosen deliberately based on the value of the tension, such that we get the best results from our edge detection method. We note the value of both of these parameters when presenting our findings.

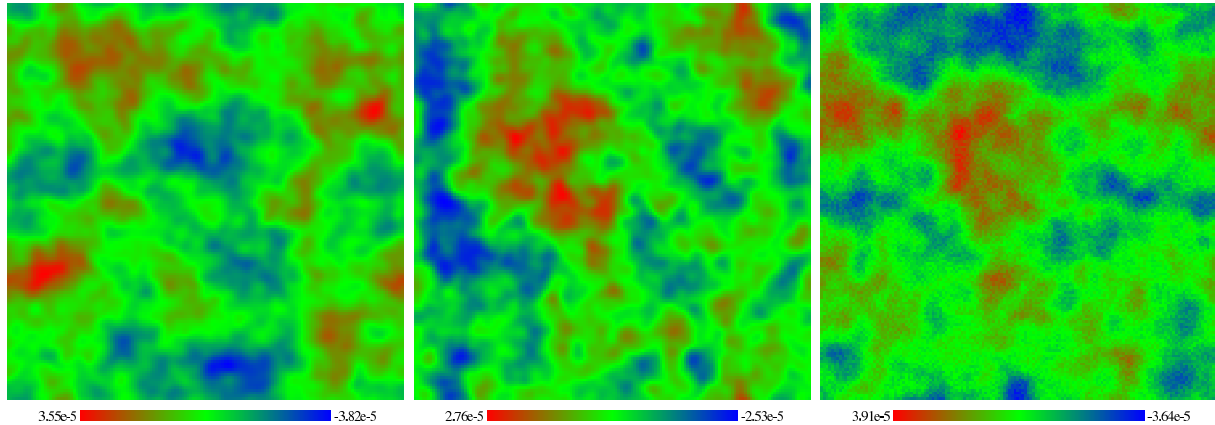


FIG. 4: Comparison of CMB maps including different components. On the left is a basic map map with Gaussian fluctuations only. In the middle is a map which includes a cosmic string component but excludes instrumental noise. On the right is a map which includes instrumental noise but excludes a cosmic string component. Note that different realizations of the Gaussian noise were used in each of the three panels. All three maps show a $2.5^\circ \times 2.5^\circ$ patch of sky at $1'$ resolution (22,500 pixels). The values of the free parameters in the cosmic string simulation were $G\mu = 6 \times 10^{-8}$ and $M = 10$. The scaling factor in the map component addition that produced the map in the middle was $\alpha = 0.987$. For the map on the right the maximum temperature fluctuation caused by the noise was taken to be $\delta T_{N,max} = 10 \mu\text{K}$.

For the SPT specific simulations, the capability of the edge detection method to make a significant detection of the cosmic string signal for different choices of the cosmic string tension is summarized in Table I. We find that our edge detection method can distinguish a signal arising from cosmic strings down to a tension of $G\mu = 5 \times 10^{-8}$. Therefore, if the edge detection method was used on ideal data from the SPT, but was unable to distinguish a difference from a theoretical data set without the effect cosmic strings, we could then impose a constraint on the cosmic string tension of $G\mu < 5 \times 10^{-8}$.

The above mentioned results were determined from simulated maps which did not contain a component of instrumental noise. To examine the effect that detector noise will have on the ability of the edge detection method to constrain the cosmic string tension, we repeat the same process described above, with the same choices for all of the parameters, but this time with instrumental noise included in the simulation of the CMB maps. As mentioned earlier, we simulate a component of white noise with a given maximum temperature change. Here, we choose the maximum temperature change caused by the instrumental noise to be $\delta T_{N,max} = 10 \mu\text{K}$, roughly corresponding to that planned for the SPT [38]. Figure 4 shows a side by side comparison of a simulated CMB map which includes instrumental noise and one which does not. The effect that the noise has on the

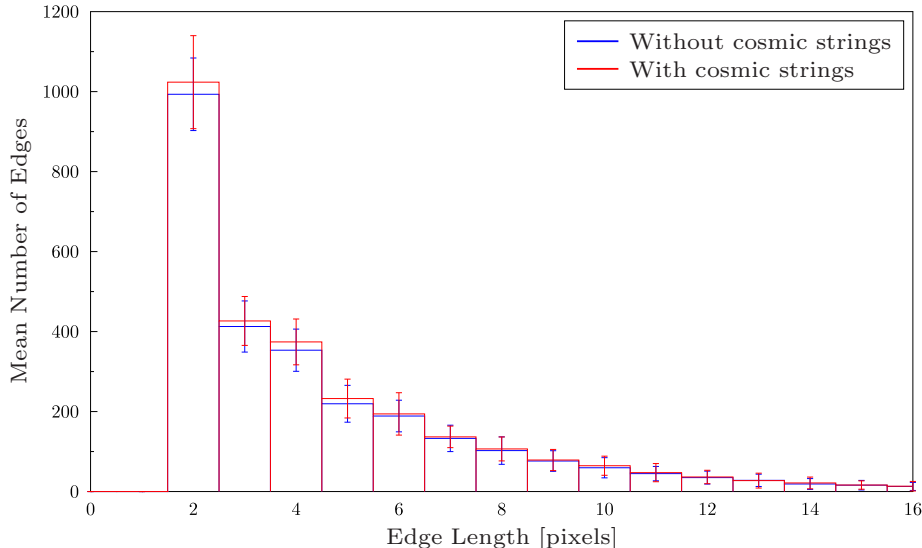


FIG. 5: Comparison of histograms for maps with and without a component of cosmic string induced fluctuations. Each histogram corresponds to a set of 40 simulated CMB maps. The angular size of each map was $10^\circ \times 10^\circ$ and the angular resolution of each was $1'$ per pixel (360,000 pixels). In the maps including a cosmic string component, the string free parameters were taken to be $G\mu < 6 \times 10^{-8}$ and $M = 10$ while the scaling factor in the map component addition was $\alpha = 0.987$. In the edge detection algorithm the gradient filter length was 5 pixels and the thresholds were $t_u = 0.25$, $t_l = 0.10$ and $t_c = 3.5$. The value of G_m was calculated using the same cosmic string tension given above. The height of each bar corresponds to the mean number of edges at that edge length. The error bars represent a spread of 3σ from the mean value, where σ is the standard deviation of the mean. Shown here are only the lengths for which the mean is greater than 3σ in both histograms.

map is clear, making it appear pixelated and non-Gaussian, yet the overall structure of the image is still visible since the temperature fluctuations caused by the noise are sub-dominant compared to the Gaussian fluctuations.

For the SPT specific simulations including instrumental noise, the results of using the edge detection method to detect a cosmic string signal are also presented in table I. We find that detector noise does not have a substantial effect, and it weakens the possible constraint that the edge detection method could place on the cosmic string tension only slightly to $G\mu < 5.5 \times 10^{-8}$.

Along with the results specific to the SPT, we explore how the constraint which could be applied by the edge detection method changes based on the specifications of the survey. For this purpose, we imagine a theoretical observatory which has the same specifications as the SPT but could map five times the amount of sky with the same resolution, that is, produce a 20,000 square degree

TABLE I: Summary of the ability of the Canny algorithm to make a significant detection of a cosmic string signal for SPT specific simulations. Shown here are the results corresponding to simulated CMB maps excluding instrumental noise as well as simulated CMB maps including instrumental noise. In the first column are different choices for the tension of the cosmic strings. In the second, third and fourth columns are the values of the scaling factor, cutoff threshold and p-value respectively, corresponding to each of the tensions. A p-value of less than 2.7×10^{-3} indicates that the simulations including cosmic strings produced significantly different results from those without cosmic strings.

String Tension ($G\mu$)	Scaling Factor (α)	Cutoff Threshold (t_c)	p-value
Without Instrumental Noise			
6.0×10^{-8}	0.987	3.5	7.19×10^{-12}
5.5×10^{-8}	0.989	4.2	6.99×10^{-4}
5.0×10^{-8}	0.991	5.5	2.39×10^{-3}
4.5×10^{-8}	0.993	6.0	9.95×10^{-3}
With Instrumental Noise			
6.0×10^{-8}	0.987	3.5	2.92×10^{-10}
5.5×10^{-8}	0.989	4.2	1.45×10^{-3}
5.0×10^{-8}	0.991	5.5	1.36×10^{-2}
4.5×10^{-8}	0.993	6.0	1.96×10^{-2}

survey of the anisotropies in the CMB. To replicate the output of a survey with this design, we instead simulate 200 separate $10^\circ \times 10^\circ$ maps at $1'$ resolution. In this hypothetical case we again choose the maximum temperature change caused by the instrumental noise to be $\delta T_{N,max} = 10 \mu\text{K}$. The analysis follows the same procedure as outlined above, and we keep the same values for all of the free parameters.

For the larger survey size, the results of using the edge detection method to detect a cosmic string signal are summarized in Table II. By increasing the survey size from that of the SPT by a factor of five, while keeping all other specifications the same, the ideal output from such an observatory could have the potential to improve the constraint on the cosmic string tension to $G\mu < 3.0 \times 10^{-8}$. When instrumental noise is included, we find that the effect on the edge detection method is in this case negligible and the possible bound remains the same as that found using simulations without instrumental noise.

TABLE II: Summary of the ability of the Canny algorithm to make a significant detection of a cosmic string signal for simulations corresponding to a hypothetical CMB survey. Shown here are the results corresponding to simulated CMB maps excluding instrumental noise and simulated CMB maps including instrumental noise. See the caption of Table I for a description of the columns.

String Tension ($G\mu$)	Scaling Factor (α)	Cutoff Threshold (t_c)	p-value
Without Instrumental Noise			
3.5×10^{-8}	0.995	8.0	1.95×10^{-5}
3.0×10^{-8}	0.997	8.8	8.16×10^{-4}
2.5×10^{-8}	0.998	9.6	7.87×10^{-3}
With Instrumental Noise			
3.5×10^{-8}	0.995	8.0	2.37×10^{-5}
3.0×10^{-8}	0.997	8.8	1.46×10^{-3}
2.5×10^{-8}	0.998	9.6	2.80×10^{-1}

VI. DISCUSSION

We have developed a method of searching for linear discontinuities in the microwave background temperature caused by the presence of cosmic strings along our line of sight to the surface of last scattering. The method which we have developed involves applying an edge detection algorithm to CMB temperature anisotropy maps in order to identify the effect of cosmic strings. We have applied our edge detection method to simulated CMB maps both including cosmic strings, and without cosmic strings, to test its ability to discriminate between the two. This then translates directly into a possible constraint on the cosmic string tension. In particular, we have focused on two different sets of simulations, one which mimics the future output coming from the SPT and one which corresponds to a theoretical survey which covers five times as much sky as the SPT with the same angular resolution. We find that the edge detection method could potentially place a bound on the cosmic string tension of $G\mu < 5 \times 10^{-8}$ for a perfect CMB observation from the SPT and that this could be lowered to $G\mu < 3 \times 10^{-8}$ for the larger survey[45]. For more realistic simulations which include instrumental noise, we find that the potential bound corresponding to the SPT weakens by only a small amount to $G\mu < 5.5 \times 10^{-8}$ while the possible bound corresponding to the theoretical survey does not change at all, and is still $G\mu < 3 \times 10^{-8}$. We consider the constraint corresponding to the SPT specific simulations which include a component of instrumental noise to be the main conclusion of this work. This possible bound is approximately an order of magnitude better than those arising from other methods which use CMB observations and approximately two

orders of magnitude better than those arising from other methods which search for the KS-effect. Therefore, we believe that using the output from the SPT along with the edge detection method has the potential to greatly improve the constraint on the cosmic string tension. This bound is not tighter than the constraints arising from current pulsar timing data, although it is competitive, falling directly within the range of values reported by different observations. Nevertheless, as mentioned in the Overview, we consider our method of constraining the tension to be more robust since we make less assumptions about some of the unknown parameters which describe the cosmic string network and its evolution. Therefore, we believe that the possible bound on $G\mu$ given above would in fact represent a stronger constraint.

We conclude that instrumental noise does not have a very major effect on the ability of the edge detection method to identify the cosmic string signal. We believe that this is an indication that the thresholding with hysteresis performs as it should, since noisy pixels could destroy the edge signal by causing large fluctuations in the gradient magnitude. Furthermore, as one can see from Figure 5, the largest difference between histograms occurs at short lengths rather than longer lengths. The instrumental noise leaves this difference in the short edge signal between maps with and without strings relatively unchanged, since the probability of a particularly noisy pixel falling on a short edge, resulting in it being incorrectly detected by the Canny algorithm, is small compared to that for longer edges. While on the topic of instrumental noise, we reiterate that we have included only a simplified white noise component in our simulations. A more complex investigation of instrumental noise would include a low frequency piece which results in stripes appearing in the final map of the CMB. Based on the method described in this paper, it is clear that striping would be crucial, since it would result in maps with more edges than that predicted by the cosmological theory and this could be confused with the effect of cosmic strings. One redeeming feature of this type of low frequency noise is that the stripes which are introduced would lie along the scanning direction, thus, when dealing with actual SPT data, it may be possible to subtract this effect out of the final map or to simply ignore edges lying along the known scanning direction in the edge detection algorithm itself. No other systematic effects due to the instrumental scanning strategy have been included in the current analysis, nor have errors due to foregrounds in the microwave sky. In future work it would be useful to investigate all types of noise as well as the removal strategies in more detail to determine if they could change the behavior of the edge detection method.

We also found that increasing the simulated survey size increases the statistical significance of the deviations between the histograms for similar values of the cosmic string tension. This behaviour is expected though, since more edge maps were used to compute the mean values in

each of the histograms and one can see from Equation (22) that the value of t scales as \sqrt{n} . While the p-values are smaller for similar tensions, the final constraint which can be levied by the larger survey is not drastically different from that corresponding to the SPT specific simulations. Increasing the survey size by 5 times only lowered the possible constraint by a factor of roughly $\sqrt{5}$. Based on this result, we conclude that the survey size does not have a major influence on the ability of the edge detection method.

When generating the simulated CMB maps, we employed a toy model of the cosmic string network which includes only straight strings and no cosmic string loops. More detailed models of the network and its evolution have been developed in other works [6, 7, 8, 44] and can be implemented numerically. Therefore, one obvious way to improve the testing method we have outlined here would be to implement one of these more complex models which would in turn produce a more realistic map of the temperature anisotropies induced via the KS-effect. On the other hand, we stress that a change of this nature would come at a large computational expense. On a similar note, it may also be useful to develop a more robust method of combining the string induced temperature anisotropies with those coming from Gaussian fluctuations, to make sure that the final simulated map agrees with other observations. Furthermore, after applying the Canny edge detection algorithm to the CMB temperature anisotropy maps, we quantify the corresponding edge map by recording the length of every edge appearing in it. As mentioned in Section IV, this is one of the simplest ways of describing the edge map, and it may be beneficial to investigate an alternative method of image comparison which provides a more powerful way of discriminating between the two edge maps. For now, we leave these improvements as the goal of future work.

While we have chosen to focus on the SPT in this work, the edge detection method is quite versatile and could be used with virtually any high resolution CMB survey. We conclude that this method presents a powerful and unique way of constraining the cosmic string tension which has the potential to perform better than current methods, or, at the very least, to provide a complimentary technique to those already in use.

Acknowledgements

We would like to thank Gil Holder and Matt Dobbs for useful discussions concerning various parts of this work. Thank you to Joshua Berger and, especially, Stephen Amsel for making their code available and for answering many questions regarding the edge detection method. We also wish to extend a big thank to Eric Thewalt for debugging some parts of the code and making many

helpful suggestions. R.B. wishes to thank Rebecca Danos for useful discussions. R.B. is supported by an NSERC Discovery Grant and by funds from the Canada Research Chairs Program.

-
- [1] A. Vilenkin and E. P. S. Shellard, *Cosmic Strings and Other Topological Defects* (Cambridge, UK: Cambridge University Press. ISBN 0521654769. pp. 578, 2000).
 - [2] M. B. Hindmarsh and T. W. B. Kibble, Rept. Prog. Phys. **58**, 477 (1995), arXiv:hep-ph/9411342.
 - [3] R. H. Brandenberger, Int. J. Mod. Phys. **A9**, 2117 (1994), arXiv:astro-ph/9310041.
 - [4] E. P. S. Shellard, Nucl. Phys. **B283**, 624 (1987).
 - [5] A. Albrecht and N. Turok, Phys. Rev. Lett. **54**, 1868 (1985).
 - [6] D. P. Bennett and F. R. Bouchet, Phys. Rev. Lett. **60**, 257 (1988).
 - [7] B. Allen and E. P. S. Shellard, Phys. Rev. Lett. **64**, 119 (1990).
 - [8] A. Albrecht and N. Turok, Phys. Rev. **D40**, 973 (1989).
 - [9] N. Turok and R. H. Brandenberger, Phys. Rev. **D33**, 2175 (1986).
 - [10] H. Sato, Prog. Theor. Phys. **75**, 1342 (1986).
 - [11] A. Stebbins, Astrophys. J. (Lett.) **303**, L21 (1986).
 - [12] P. D. Mauskopf et al. (Boomerang), Astrophys. J. **536**, L59 (2000), arXiv:astro-ph/9911444.
 - [13] C. L. Bennett et al. (WMAP), Astrophys. J. Suppl. **148**, 1 (2003), arXiv:astro-ph/0302207.
 - [14] L. Perivolaropoulos, Astrophys. J. **451**, 429 (1995), arXiv:astro-ph/9402024.
 - [15] J. Magueijo, A. Albrecht, D. Coulson, and P. Ferreira, Phys. Rev. Lett. **76**, 2617 (1996), arXiv:astro-ph/9511042.
 - [16] U.-L. Pen, U. Seljak, and N. Turok, Phys. Rev. Lett. **79**, 1611 (1997), arXiv:astro-ph/9704165.
 - [17] R. H. Brandenberger and C. Vafa, Nucl. Phys. **B316**, 391 (1989).
 - [18] N. T. Jones, H. Stoica, and S. H. H. Tye, Phys. Lett. **B563**, 6 (2003), arXiv:hep-th/0303269.
 - [19] R. Jeannerot, J. Rocher, and M. Sakellariadou, Phys. Rev. **D68**, 103514 (2003), arXiv:hep-ph/0308134.
 - [20] M. Wyman, L. Pogosian, and I. Wasserman, Phys. Rev. **D72**, 023513 (2005), arXiv:astro-ph/0503364.
 - [21] L. Pogosian, S. H. H. Tye, I. Wasserman, and M. Wyman, Phys. Rev. **D68**, 023506 (2003), arXiv:hep-th/0304188.
 - [22] L. Pogosian, S. H. H. Tye, I. Wasserman, and M. Wyman (2008), arXiv:0804.0810 [astro-ph].
 - [23] A. A. Fraisse, JCAP **0703**, 008 (2007), arXiv:astro-ph/0603589.
 - [24] U. Seljak, A. Slosar, and P. McDonald, JCAP **0610**, 014 (2006), arXiv:astro-ph/0604335.
 - [25] N. Bevis, M. Hindmarsh, M. Kunz, and J. Urrestilla, Phys. Rev. **D75**, 065015 (2007), arXiv:astro-ph/0605018.
 - [26] N. Bevis, M. Hindmarsh, M. Kunz, and J. Urrestilla, Phys. Rev. Lett. **100**, 021301 (2008), arXiv:astro-ph/0702223.
 - [27] T. Damour and A. Vilenkin, Phys. Rev. **D71**, 063510 (2005), arXiv:hep-th/0410222.

- [28] F. A. Jenet et al., *Astrophys. J.* **653**, 1571 (2006).
- [29] A. A. Fraisse (2005), arXiv:astro-ph/0503402.
- [30] N. Kaiser and A. Stebbins, *Nature* **310**, 391 (1984).
- [31] A. Vilenkin, *Phys. Rev.* **D23**, 852 (1981).
- [32] R. Moessner, L. Perivolaropoulos, and R. H. Brandenberger, *Astrophys. J.* **425**, 365 (1994), arXiv:astro-ph/9310001.
- [33] J. C. R. Magueijo, *Phys. Rev. D* **46**, 1368 (1992).
- [34] E. Jeong and G. F. Smoot (2006), arXiv:astro-ph/0612706.
- [35] A. S. Lo and E. L. Wright (2005), arXiv:astro-ph/0503120.
- [36] J. Canny, *IEEE Trans. Pattern Anal. Mach. Intell.* **8**, 679 (1986), ISSN 0162-8828.
- [37] S. Amsel, J. Berger, and R. H. Brandenberger, *JCAP* **0804**, 015 (2008), arXiv:0709.0982 [astro-ph].
- [38] J. E. Ruhl et al. (The SPT) (2004), arXiv:astro-ph/0411122.
- [39] M. J. White, J. E. Carlstrom, and M. Dragovan, *Astrophys. J.* **514**, 12 (1999), arXiv:astro-ph/9712195.
- [40] E. Komatsu et al. (WMAP) (2008), arXiv:0803.0547 [astro-ph].
- [41] J. R. Bond and G. Efstathiou, *Mon. Not. Roy. Astron. Soc.* **226**, 655 (1987).
- [42] C. L. Reichardt et al. (2008), arXiv:0801.1491 [astro-ph].
- [43] L. Perivolaropoulos, *Phys. Lett.* **B298**, 305 (1993), arXiv:hep-ph/9208247.
- [44] A. A. Fraisse, C. Ringeval, D. N. Spergel, and F. R. Bouchet (2007), arXiv:0708.1162 [astro-ph].
- [45] Note that the dependence of the limit as a function of angular resolution was studied in [37]